Original Article

AUTOMATED GLAUCOMA DETECTION SYSTEM BASED ON TWIN STAGE SEGMENTATION AND MACHINE LEARNING

R. Revathi[1], Dr. G. Jagatheeshkumar[2]

[1] Research Scholar, PG & Research Department of Computer Science, Karuppannan Mariappan College, Muthur, Tamilnadu, India.
[2] Associate Professor and Head, PG & Research Department of Computer Science, Karuppannan Mariappan College, Muthur, Tamilnadu, India.

DOI: 10.47750/pnr.2023.14.02.206

Abstract

Glaucoma is a serious threat and it causes blindness and it ranks third in India. Early identification of glaucoma sickness prevents eye disorders from worsening. Due to the need for early illness detection tools to aid in screening and management, retinal image analysis has attracted keen interest. This article presents an automated glaucoma detection system, which is based on machine learning. The retinal images are denoised and contrast enhanced, followed by which the Optic Disc and Cup are extracted. The Complete Local Binary Pattern (CLBP) and contourlet features are extracted to train the Extreme Learning Machine (ELM) classifier. The ELM differentiates between the glaucomatous and non-glaucomatous images. The experimental findings are evaluated with the existing methods, and it is found that the proposed work is superior in terms of standard performance measures.

Keywords: Retinal images, glaucoma detection, machine learning, classification.

1. Introduction

Glaucoma is a prevalent eye condition that is brought on by an elevation in the eye's intraocular pressure. If left untreated, it can result in permanent blindness. This condition may happen due to the race, age, refractive error, Optical Disc (OD), and Retinal Nerve Fibre Layer (RNFL) of a patient [1]. The OD is an essential predictor of glaucoma, the most prominent indicators of which are alterations such as cupping and thinning of the RNFL. Glaucoma can be recognized in its early stages and potentially avoided complications if one takes advantage of the changes that occur in OD.

Hence, a glaucoma detection framework has to be designed, which can prove its resistance towards OD variability, since different kinds of glaucoma have OD manifestations that are quite similar to one another. Different clinical researches study the association of glaucoma with the OD concerning its structural alterations, such as cupping, thinning, excavation and disc bleeding. These studies have been undertaken in order to shed light on the nature of this relationship. In [2], an experiment of this kind that was conducted before the last two decades discuss numerous OD characteristics with their ranking for the early glaucoma detection.

Additionally, a latest study demonstrates that constrictive ODs are present in juvenile members who have Central Retinal Vein Occlusion (CRVO) [3-6], which is the main cause of glaucoma. The clinical significance of ODs in glaucoma detection is thoroughly recognized by the ophthalmology research community, as demonstrated by these trials.

A varied morphological appearances of bleeding patterns that appear on the OD surface may induce difficulty to classify glaucomatous disc alterations. Cup to Disc Ratio (CDR), also known as the ratio of Vertical Cup Diameter (VCD) to Vertical Disc Diameter (VDD), is one of the common measurements used for glaucoma detection. [2] CDR is computed as the fraction of VCD by VDD. A greater CDR indicates an increased likelihood of developing glaucoma. Yet, VCD is a subjective measurement, and estimating the shape of the OD from fundus images, particularly from images obtained through the boundary of the OD, can be challenging.

It is particularly difficult to pinpoint the OD's boundary, during the eye for the purpose of identifying cup forms. To determine CDR, first the OD region and then the Optic Cup (OC) region are segmented, and then the VCD to VDD ratio is calculated. Measurement-based approaches are known as the older methods for automated glaucoma screening [7–10]. These methods segmented the ODs and cups and then the CDR is computed. It is a nontrivial task to perform segmentation of ODs and cups, while erroneous segmentations might lead to false detections if they are not performed accurately.

Understanding the seriousness and severity of this disease, this article attempts to present an auto-detection system for glaucoma with the aid of machine learning. The glaucomatous and non-glaucomatous areas are classified by employing different phases of image processing such as image enhancement, segmentation of OD and cup, feature extraction and classification. The work highlights are presented as follows.

- The automated glaucoma detection systems can help physician in effective diagnosis of the disease with better accuracy rates.
- Effective segmentation of optic cup and disc helps in attaining better detection accuracy rates.
- Extraction of potential features paves way for better classification of glaucomatous and non-glaucomatous areas.

This paper is structured as follows. Section 2 analyzes recent literature, while section 3 explains the proposed work. Section 4 analyzes the suggested work and section 5 draws conclusions.

2. Review of literature

This section discusses the existing literature concerning glaucoma detection.

In [7], an ML-based glaucoma detection technique is presented. After pre-processing, CED was used to segment blood vessels. The suspected sample's blood arteries were segmented morphologically. Next, final feature computation was done using FEM. Support vector machine (SVM) training employed computed features for categorization. This study works better with noisy samples, however computational complexity is involved. The authors of [8] presented an algorithm to detect optic cups from retinal fundus data with the Glowworm Swarm Optimization. This work can identify glaucoma but not calculate cup-to-disc ratio. A fine sub-band imaging is used from samples to identify glaucoma in [9]. LS-SVM was trained using SS-QB-VMD calculated features. This work detects glaucoma well, but accuracy needs improving.

A framework for glaucoma lesions is presented in [10]. OD and OC were segregated by employing pixel-based threshold and watershed transformation after image pre-processing. The cup is divided by disc pixels to compute CDR. This approach recognizes glaucomatous regions well, however the variations in scale and rotation is difficult to handle. An automated framework based on Machine Learning (ML) to determine the vertical cup-to-disk ratio (VCDR) from fundus images is presented in [11]. Initial OD localization used vascular and disk-selective COSFIRE filters. The OD and OC regions were then classified using GMLVQ. This work proves better glaucoma detection accuracy, but is not resilient to noisy samples.

A CNN framework to detect glaucoma is presented in [12]. After pre-processing, the deep features are computed by MobileNetV2, which were then categorized as healthy or glaucoma-affected. Better computationally, but model training requires more data. In [13], DL was used to classify glaucoma-affected samples from healthy images. For dependable keypoint extraction from input images, evolutionary convolutional network (ECNet) was introduced. The retrieved key points were then used to train KNN, SVM, BPNN, and ELM to accomplish the classification process. The SVM classifier achieves the greatest results, but at a higher computational cost.

In [14], the authors presented system for automated glaucoma detection and categorization based on DL. Le-Net was initially used to identify RoI from input images. OD and OC segmentation was done using U-Net. SVM, NN, and Adaboost classifiers were used for classification. Combining the results of SVM, NN, and Adaboost classifier increase the processing cost [14]. In [15], a CNN-based framework is presented with DOE-based hyper parameters. The study [15] improves glaucoma classification, but the approach lacks standard datasets. In [16], glaucomatous fundus areas are detected by ResNet-50, however they may not be resilient against noisy and blurry images.

DenseNet-201 [17] is another DL-based system for glaucoma recognition. This work is computationally better, but performance needs improving. The authors of [18] presented an ensemble OD and OC approaches. The deep features of AlexNet, ResNet-50, and ResNet-152 are fused to classify between the normal and glaucoma affected areas. This computationally intensive system improves glaucoma classification performance. In [19], a Mask-RCNN is developed to group OD and OC fundus lesions. Mask-RCNN used DenseNet-77 as a backbone to extort deep keypoints from the input image. In [19], a technique segmented glaucoma effectively, but results need improving. In [20], the authors developed Fast Region-based Convolutional Neural Network (FRCNN) technique with fuzzy k-means (FKM) clustering. The glaucoma segmentation is proven to be better but at high cost.

In [21], a combined OD/OC segmentation is framed as a semantic pixel-wise labelling problem. A Cup Disc Encoder Decoder Network (CDED-Net), based on SegNet is presented in [22], where this work fills the gap between encoder and decoder blocks semantically with the feature information. This work carries out OD segmentation on datasets such as Drishti-gs, RIM-ONE, and REFUGE. In [24], Recurrent Fully Convolution Network (RFC-Net) captures high-level visual information and fine edges with multiscale input, recurrent units and numerous output layers. Different recurrent units, each one with a distinct stacking of basic convolutional layers, are used for segmentation evaluation of the OD and cup. Experimental results indicate stacked recurrent units achieve 0.9795 is the accuracy for combined disc and cup segmentation on the Drishti-gs dataset.

A disc-aware ensemble network (DENet) is utilized as a binary classifier for screening glaucoma in [24]. This network uses fundus image, disc-cropped fundus image, disc segmentation map, and disc polar transform classification streams. The four streams' classification results are averaged to get a single value. This network achieves top AUC values on the SCES and SINDI [25] datasets. An adversarial learning framework called pOSAL [26] segments ODs and OCs based on their morphologies. An unsupervised domain adaptation is employed to segment heterogeneous datasets. RoIs derived from source and target images are used. OD and OC masks are predicted by an adversarial segmentation network. A discriminator uses adversarial learning to anticipate source and target images. For segmentation network generalization, adversarial loss is computed on target images. This network's REFUGE DC is 0.946.

Motivated by these works, this article presents an auto detection model for glaucoma with the help of Machine Learning (ML) approach, which ensures better detection rates with reasonable sensitivity and specificity rates.

3. Proposed auto-detection model for glaucoma detection

Glaucoma is one of the serious illnesses, which when left untreated leads to blindness. The loss due to this disease is irreversible and hence, it is necessary to carry out periodical screening. In order to detect glaucoma, the localization of OD and cup is essential. Initially, the optic disc is segmented and is followed by cup. The overall flow of the work is shown in figure 1.

Fig.1. Overall flow of the proposed glaucoma detection system

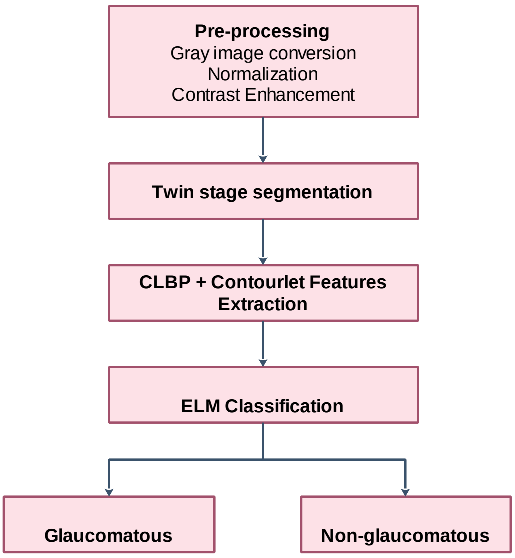

Pre-processing the images helps in segmenting the area of interest effectively. Potential features are extracted from the segmented regions, so as to classify between the glaucomatous and non-glaucomatous samples. The following sub-sections explain all the involved processes.

3.1 Data Collection

The retinal fundus images are collected from the public datasets such as HRF and RIM-ONE. The HRF dataset contains the 15 normal and 15 glaucomatous images. The RIM-ONE dataset contains 158 images, out of which 84 images are labelled normal, 39 are glaucomatous and the remaining are glaucoma-suspect. These datasets are downloaded from the links [26,27].

3.2 Image Pre-processing

Denoising and enhancing the image are the primary concerns of the image preprocessing activity in the vast majority of instances. It has been shown that the results are more believable when the images are preprocessed in a competent manner. During this stage, we will work to clean up the supplied image and improve its quality. First, the images that have been collected are given standardization, and then the CLAHE algorithm is employed for contrast enhancement of the images. The impulse noise, which is typically present in retinal images, can be eliminated using the normalization procedure. The following equation is what is used to carry out the normalization process and the pre-processed image is shown in figure 2.

Fig.2. (a) Original Image (b) Gray image (c) pre-processed image

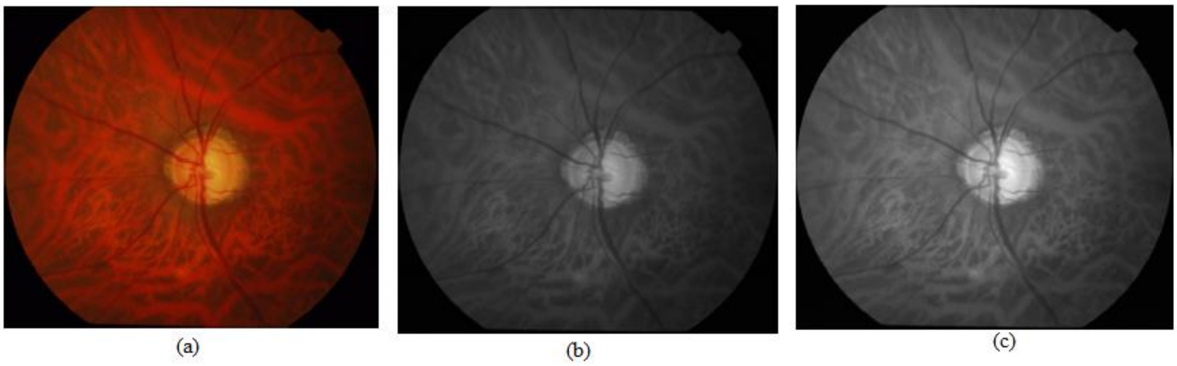

$$M_{img} = \left(O_{img} - \min\right) + \frac{i_{max} - i_{min}}{max - min} + i_{min} \quad (1)$$

In the above equation, O_{img} and M_{img} are the input and modified images respectively. The intensity range of input and modified images are represented as (max,min) and (i_{max}, i_{min}) respectively. The normalized image falls in the intensity range between 0 and 255. The CLAHE improves visual contrast locally. This approach boosts an image's brightness so details can be seen. CLAHE boosts image brightness without causing saturation. CLAHE is simple and effective.

3.3 Segmentation of OD and cup

The suggested technique separates the disc and cup from images using rough and fine segmentation. Rough segmentation considers image edges and details. The outlines are initially represented via the level set approach, based on the changing energy function, as represented in equation 2.

$$E(\emptyset) = -W_1 \int \frac{(Im - GL)HF(\emptyset)did}{ID} + W_2 \int \frac{GR|\nabla HF(\emptyset)|did}{ID} \quad (2)$$

$\emptyset$ is the contour C's empty set embedding function. Im is the segmented image, $HF(\emptyset)$ is the Heaviside function, and ID is image domain. W_1 and W_2 are balancing attributes for the image gradient (GR), which is $GR(|\nabla|Im)$. In the first portion of the equation, GL denotes the disc's grey level. This component supports edges with grey values above GL. Sample segmentation results are displayed in figure 3.

Fig.3. (a) Original image (b) segmented OD (c) Ground truth image

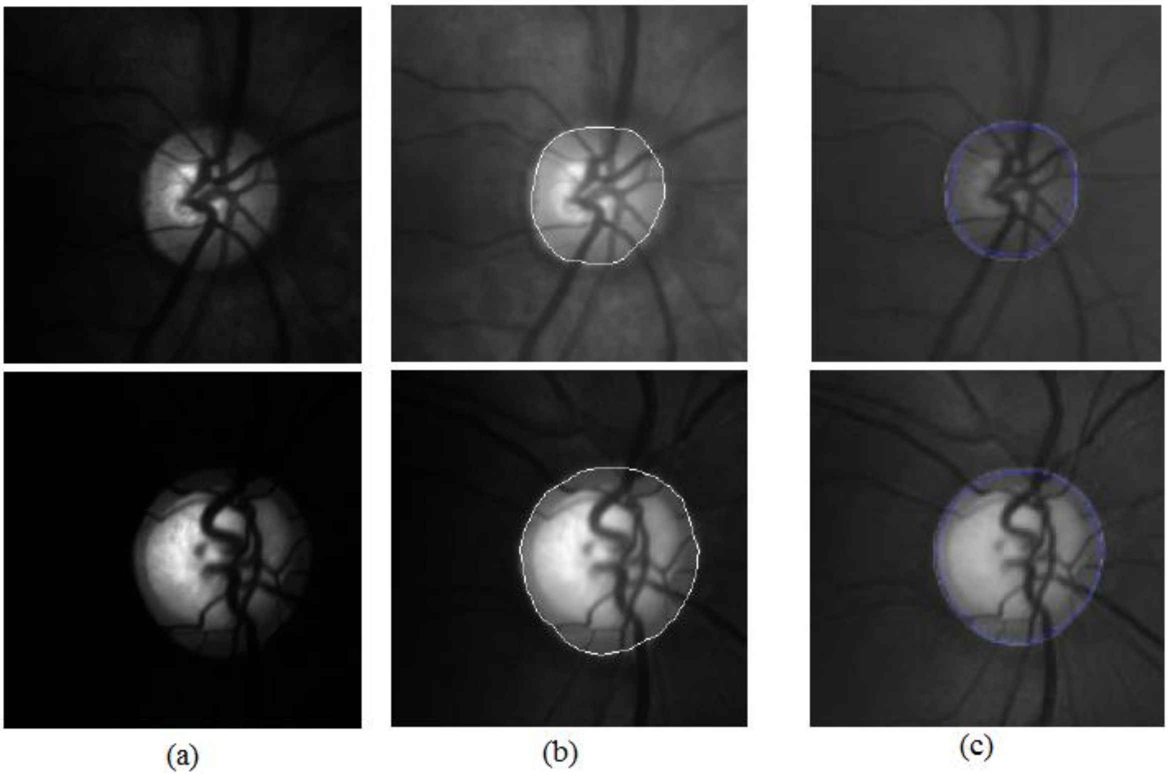

Second component of equation is geodesic active contour function for level set boundary. Overlap prevents this function from detecting the disc perfectly. Consider both global and local facts of the area to solve this problem, as in equation 3.

$$L_i = \int_{I(CN)} (AF(I) - I - v_1)^2 dCN + \int_{O(CN)} (AF(I) - I - v_2)^2 dCN \quad (3)$$

$AF(I)$ is the average filter, and $AF(I) - I$ is the average inner $I(CN)$ and outer $O(CN)$ contour intensities. Consider both the inner and outer contour sections to address overlap. This idea effectively extracts discs from images, and the retrieved areas are processed with feature extraction.

3.4 CLBP and Contourlet Feature Extraction

3.4.1 CLBP

The step known as "feature extraction" is considered to be the most important part of any automated system. During this phase, significant features are extracted from the images in order to identify any irregularities. The extraction of the features is accomplished by combining the CLBP and contourlet methods. CLBP is an improvement on LBP [28] and is an effective texture descriptor. A local region is represented by CLBP through the utilization of a center pixel and the Local Difference Sign-Magnitude Transform (LDSMT). LDSMT is the process of subtracting the magnitude from the pixel values while taking into account the local center pixel. The binary global threshold map has been given the label CLBP_Centre ($CLBP_C$), and it is used to characterize the centre pixel. CLBP_Sign ($CLBP_S$), CLBP_Magnitude $CLBP_M$), and CLBP Centre ($CLBP_C$) are the three important components that make up the CLBP.

$CLBP_S$ is an abbreviation that stands for the pixel value's sign, which can be determined by difference between the central pixel and local pixel values. The symbol could have a positive or a negative connotation. $CLBP_M$ represents the magnitudinal difference between the central and the value of the local pixels. In a similar manner, $CLBP_C$ is the value that is obtained by subtracting the average value of the central pixel from the local pixel's value. $CLBP_S$ is comparable to LBP and can be calculated using the same formula.

$$CLBP_{S_{P,R}} = \sum_{p=0}^{p-1} s(g_p - g_c) 2^p \quad (4)$$

where the central pixel's gray level is denoted by g_c, and the value of the surrounding pixels, denoted by g_p, are taken into account. P is the number of pixels that make up the neighborhood, and R is the distance from the center of the neighborhood window. The following condition will decide whether or not the pixel value has a positive or negative sign.

$$s(a) = \begin{cases} 1 & if\ a \geq 0 \\ 0 & if\ a < 0 \end{cases} \quad (5)$$

$$CLBP_{M_{P,R}} = \sum_{p=0}^{p-1} t(m_p, c) 2^p \quad (6)$$

$$t(x,c) = \begin{cases} 1 & x \geq c \\ 0 & x < c \end{cases} \quad (7)$$

The threshold, denoted by c, has a variable value, and the magnitude, denoted by m_p, is given. The following equation can be used to determine $CLBP_C$.

$$CLBP_{C_{P,R}} = t(g_c, c_l) \quad (8)$$

where c_l is the typical level of grey for the entire image. It is possible to club all three of these entities either by combining all three of them at once or by combining two of the entities, then the third.

3.4.2 Contourlet

Image representation affects feature extraction. Multiresolution, localisation, directionality, and anisotropy are important for image representation. Multiresolution allows digital images at all resolutions (coarse to fine). Both spatial and frequency domains must localize image components. Image representation should allow multiple directional orientations. The image representation technique must capture contours using multiple forms with aspect ratio. Wavelets provide multiresolution and localisation. Image representation techniques must meet all standards.

Curvelets meet the requirements, however they are better at representing continuous images than discrete ones. Contourlets, a multidirectional multiresolution transform, solve this problem. Conrourlet transforms are fixed by nature and applicable to any image processing task. Several transforms offer multidirection and multiresolution, although not at the same scale. Contourlets give iterated filter banks, making them more efficient than similar transforms.

Contourlet merges Laplacian Pyramid (LP) and Directional Filter Bank (DFB). The high frequency components are collected by DFB and the low-frequency components are deleted. Consider an LP input image $x_0[n]$. This stage produces K bandpass images, seen below.

$$y_k[n]; k = (1,2, \dots K) and\ x_K[n] \tag{9}$$

$y_k[n]; k = (1,2, \dots K)$ is the fine-to-coarse image, and $x_K[n]$ is the lowpass image. The k^{th} level of LP subdivides the input image $x_{k-1}[n]$ into $x_k[n]$ and $y_k[n]$ respectively. Every bandpass image $y_k[n]$ is subdivided by a degree of d_k to 2^{d_k}bandpass directional images.

$$a_{k,l}^{(d_k)}[n]; \quad k = (0,1, \dots, 2^{d_k} - 1) \tag{10}$$

Hence, contourlet is used to extract features from inputs.

The aim of this phase is to frame a feature vector by merging CLBP and contourlet, while focussing to minimize false positive and false negative rates. This work starts feature extraction via CLBP. The texture features are computed by varying P and R. Depending on P and R, the window size affects the feature count. The GLCM features are derived from the sub-bands using two-level contourlet. The contourlet is applied on the segmented image using DFB in 3 scales. GLCM is used because it builds the spatial link between pixels and texture.

GLCM is a $GL \times GL$ sized square matrix, which is the total number of image grey intensities. Consider an image element (a, b) at (x, y) with intensity I_i. The pixel at $(x + dx, y + dy)$ has grey level intensity I_j. dx and dy show scale and orientation. Weighing each co-occurrence matrix yields contourlet features. The combined values comprise the feature set. The GLCM properties being considered are autocorrelation, contrast, correlation, dissimilarity,energy, homogeneity and inertia.

I level contourlet creates 2 sub-bands and II level contourlet produces 4 sub-bands when applied to an input image. First level has 4×120 elements, second level has 16×120. The combined matrices have 20×120 entries. 3 matrices with a single pixel offset occur at 0,45 and 90 degrees. For every image, three 8×8 co-occurrence matrices are produced. This work computes 21 components from 14 attributes and 7 GLCM features for 3 matrices. CLBP's feature matrix varies with P and R. After forming feature vectors, classification begins.

3.4 Glaucoma Detection by ELM

ELM is a fast-learning classifier [29]. The classifier works after training and testing. Training requires learning through feature vectors. With this knowledge, the classifier can distinguish between normal and abnormal images during testing.

Let there be A_{TS} training samples as denoted by (s_i, t_i), where $s_i = [s_{i1}, s_{i2}, s_{i3}, \dots, s_{in}]^T \in D^n$, where s_i is the i^{th} training entity having n dimensions. $tk_i = [tk_{i1}, tk_{i2}, tk_{i3}, \dots, tk_{im}]^T \in D^m$ that represents the i^{th} training label with m dimensions. Here, m is the count of classes and the Single hidden Layer Feed-Forward Neural Network (SLFN) is formed with an activation function $act(x)$ possessing NR neurons, as in eqn.7.

$$\sum_{i=1}^{NR} \mu_i(wt_i . s_i + c) = r_j; j = 1,2,\dots,n \qquad (11)$$

In the preceding equation, wt_i is the weights given by $wt_i = [wt_{i1}, wt_{i2}, \dots, wt_{in}]^T$ and it interconnects the i^{th} hidden neuron with the input neurons. The weight vector links the i^{th}hidden neuron to the output neurons via bias $(bias_i)$. The SLFN is represented as follows.

$$\sum_{i=1}^{NR} \mu_i act(wt_i . s_i + bias_i) = tk_i; i = 1,2,\dots,n \qquad (12)$$

HDL is the hidden layer output matrix of the classifier, therefore the i^{th} column holds the i^{th} hidden neuron output vector with regard to input $s_{i1}, s_{i2}, \dots, s_{in}$.

$$HDL = \begin{bmatrix} act(wt_1 . s_1 + bias_i) & \dots & act(wt_{NR} . s_1 + bias_G) \\ \vdots & \vdots & \vdots \\ act(wt_1 . s_n + bias_i) & \dots & act(wt_{NR} . s_n + bias_G) \end{bmatrix} \qquad (13)$$

$$\mu = \begin{bmatrix} \mu_1^T \\ \vdots \\ \mu_{NR}^T \end{bmatrix} \qquad (14)$$

$$TK = \begin{bmatrix} tk_1^T \\ \vdots \\ tk_n^T \end{bmatrix} \qquad (15)$$

The matrix format representation is as follows.

$$HDL\mu = TK \qquad (16)$$

The norm least-square solution calculates output weights.

$$\mu = HDL^{\dagger}TK \qquad (17)$$

$HDL^{\dagger}$ is the Moore-Penrose generalized inverse of HDL. ELM training requires m classes, $act(x)$, and NR hidden neurons. The ELM is given a training set $Tr_{set} = \{(s_i, t_i) | s_i \in D^n, t_i \in D^m; i = 1,2,\dots,N\}$ during the knowledge-gaining phase. Equation 17 describes how to train.

During testing, the test image undergoes all the preceding steps. By including rich elements, the work's goal is achieved. This work takes less time because it doesn't entail sophisticated computations. The proposed approach ensures dependability, and its performance is analyzed below.

4. Results and discussion

The proposed glaucoma detection approach operates consistently across two datasets. The experiment is run in MATLAB 2021 on a stand-alone i7 computer with 8 GB RAM. The proposed method's accuracy (Det_{acc}), sensitivity (Det_{sen}), and specificity (Det_{spe}) are evaluated. Their corresponding formulae are presented in the following equations.

$$Det_{acc} = \frac{TP+TN}{TP+TN+FP+FN} \times 100 \qquad (18)$$

$$Det_{sen} = \frac{T_p}{T_p+F_n} \times 100 \qquad (19)$$

$$Det_{spe} = \frac{T_n}{F_p+T_n} \times 100 \qquad (20)$$

False negatives decrease as sensitivity increases. As specificity increases, false positives decrease. Achieving better sensitivity and specificity rates are difficult, when compared to accuracy rates. This work's experimentation is done in three aspects, such that the proposed segmentation, feature extraction, and classification algorithms are tested. The proposed glaucoma detection system's performance is compared against existing methods.

4.1 Performance evaluation w.r.t segmentation techniques

Two databases are utilized to check the effectiveness of the disc and cup segmentation. Segmentation outcomes affect glaucoma detection system accuracy, while it also reduces computing time and complexity by confining operations to segmented regions. The following table shows the segmentation results from this experiment utilizing twin segmentation. The results are shown by comparing single-stage and twin-stage segmentation.

Table 1: Results by varying segmentation algorithms

Database	Det_{acc} (%)		Det_{sen} (%)		Det_{spe} (%)		Time (ms)	
	Single Seg	Twin Seg	Single Seg	Twin Seg	Single Seg	Twin Seg	Single Seg	Twin Seg
HRF	97.3	**98.8**	92.7	**97.8**	90.7	**96.2**	2215	**2387**
RIM-ONE	95.6	**98.6**	93.4	**97.2**	91.6	**97.3**	2476	**2672**
Average	96.4	**98.7**	93	**97.5**	91.1	**96.7**	2728	**2350**

According to the findings of the investigation, the performance of the twin stage segmentation method is found to be superior to that of the single stage segmentation method. In addition, the work that has been planned will complete the procedure in a time frame that is acceptable. In the next section, we will test the performance of the suggested method by using a variety of different ways to extract features.

4.2 Performance evaluation w.r.t feature extraction techniques

The effectiveness of the glaucoma detection method is partially determined by the results of the second significant phase, which is the extraction of features, where CLBP+Contourlet features are utilized in this study. The performance of these individual methods is compared to the performance of these features when they are merged together. During the training process, the ELM classifier makes use of the features that were extracted. The following is a tabular representation of the outcomes of the experiment.

Table 2. Results by varying feature extraction techniques

Database	Det_{acc} (%)			Det_{sen} (%)			Det_{spe} (%)			Time (ms)		
	Contourlet	CLBP	Contourlet+CLBP	Contourlet	CLBP	Contourlet+CLBP	Contourlet	CLBP	Contourlet+CLBP	Contourlet	CLBP	Contourlet+CLBP
HRF	95.4	96.3	**98.8**	84.3	89.2	**97.8**	**82.7**	87.2	**96.2**	**2243**	**2486**	**2215**
RIM-ONE	91.8	93.8	**98.6**	**82.7**	87.6	**97.2**	**81.7**	84.6	**97.3**	**2136**	**2246**	**2286**

Average	93.6	95.05	**98.7**	83.5	88.4	**97.5**	82.2	85.9	**96.7**	2189	2366	**2250**

Based on the findings of the experiments, it can be seen that the performance of CLBP and contourlet is improved when used together as opposed to when either method is used independently. The fact that the retrieved features are more descriptive is the primary justification. The performance of the suggested method is evaluated once again to demonstrate that the ELM classification was appropriate, and the results of those evaluations are reported in the following section.

4.3 Performance evaluation w.r.t classification techniques

In this section, the performance of the proposal is evaluated using a variety of different classifiers. The effectiveness of the ELM classifier is evaluated in comparison to that of other individual classifiers, such as the k-Nearest Neighbour (k-NN) and the Support Vector Machine (SVM). The following is a presentation of the outcomes of the experiment:

Fig.3. Performance evaluation on HRF

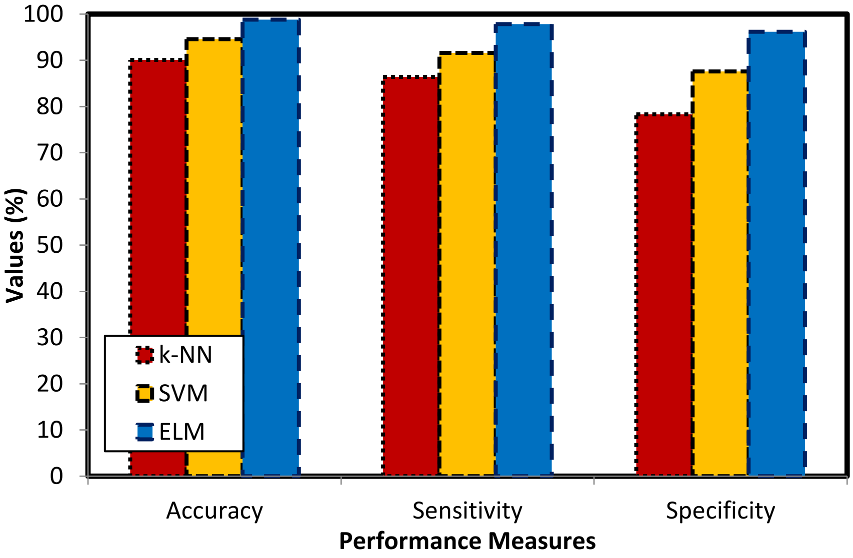

Fig.4. Performance evaluation on RIM-ONE

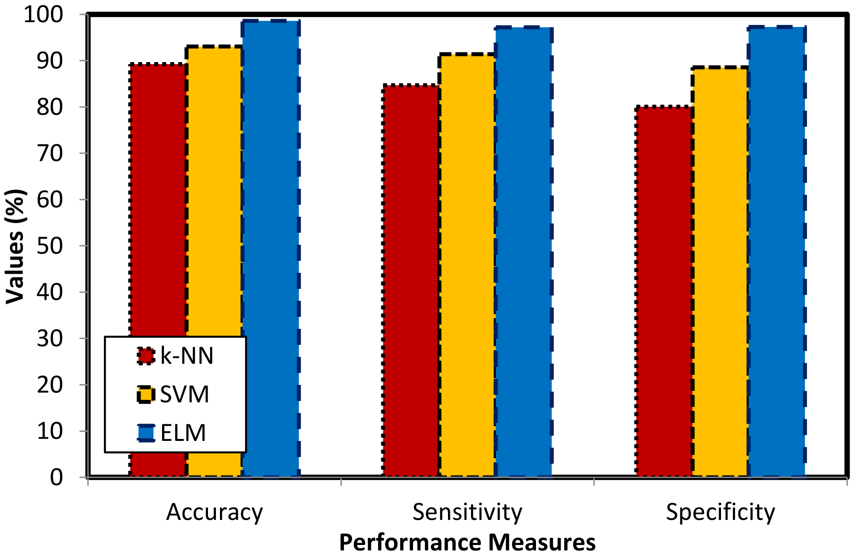

When the findings were examined, it was discovered that the performance of the classification was superior to that of the other classifiers that were compared. The efficiency of pre-processing, improved segmentation, and the successful extraction of relevant characteristics are the primary contributors to the improved glaucoma detection rates. It has been demonstrated that ELM is a more accurate classifier and has a strong capacity for learning.

4.4 Performance evaluation against state-of-the-art glaucoma detection techniques

The performance of the suggested method is evaluated in comparison to other comparable cutting-edge strategies for glaucoma detection, such as morphologically based [7] and glow-worm swarm optimization technique [8]. The following is a presentation of the results of the experiments as well as a comparative analysis of the proposed method.

Table 3. Analysis against the existing approaches

Database	Det_{acc} (%)			Det_{sen} (%)			Det_{spe} (%)			Time (ms)		
	[7]	[8]	Prop	[7]	[8]	Prop	[7]	[8]	Prop	[7]	[8]	Prop
HRF	97.3	98.7	**98.8**	92.7	95.9	**97.8**	90.7	92.8	**96.2**	2589	2389	**2215**
RIM-ONE	95.6	96.3	**98.6**	93.4	95.2	**97.2**	91.6	92.7	**97.3**	2868	2634	**2486**
Average	96.4	97.5	**98.7**	93	95.5	**97.5**	91.1	92.7	**96.7**	2728	2511	**2350**

The findings of the experiments make it abundantly clear that the proposed strategy beats the conventional methods in terms of the accuracy, sensitivity, and specificity rates it achieves. When compared to the other ways, the amount of time taken by this work is also minimal.

5. Conclusions

This article presents an automated glaucoma detection system for differentiating between the glaucomatous and non-glaucomatous images. The complete work is segregated into four significant phases, where the initial phase intends to remove noise and enhance the contrast of the image. A twin-stage segmentation procedure is performed for extracting the disc and cup regions, which is then followed by the extraction of CLBP and contourlet features. The ELM classifier is then trained with the extracted features and the glaucomatous and non-glaucomatous images are classified. In future, this work is planned to be extended to detect diabetic retinopathy as well.

References:

[1] R. J. Casson, G. Chidlow, J. P. Wood, J. G. Crowston, and I. Goldberg, “Definition of glaucoma: clinical and experimental oncepts,” Clinical & Experimental Ophthalmology, vol. 40, no. 4, pp. 341–349, 2012.

[2] J. B. Jonas, A. Bergua, P. Schmitz-Valckenberg, K. I. Papastathopoulos, and W. M. Budde, “Ranking of optic disc variables for detection of glaucomatous optic nerve damage,” Investigative Ophthalmology & Visual Science, vol. 41, no. 7, pp. 1764–1773, 2000.

[3] M. Fingeret, F. A. Medeiros, R. Susanna Jr., and R. N. Weinreb, “Five rules to evaluate the optic disc and retinal nerve fiber layer for glaucoma,” Optometry-Journal of the American Optometric Association, vol. 76, no. 11, pp. 661–668, 2005.

[4] S. Dubey and M. Gandhi, “Evaluation of the optic nerve head in glaucoma,” Journal of Current Glaucoma Practice, vol. 7, no. 3, pp. 106–114, 2013.

[5] S. Senthil, M. Nakka, V. Sachdeva, S. Goyal, N. Sahoo, and N. Choudhari, “Glaucoma mimickers: a major review of causes, diagnostic evaluation, and recommendations,” Seminars in Ophthalmology, vol. 36, no. 8, pp. 692–712, 2021.

[6] S. Lei, M. Wan, N. Tehrani, A. Reginald, and K. Mireskandari, “Optic disk anatomical features of children with central retinal vein occlusion,” Journal of American Association for Pediatric Ophthalmology and Strabismus, 2021.

[7] Shoba, S.G.; Therese, A.B. Detection of glaucoma disease in fundus images based on morphological operation and finite element method. Biomed. Signal Process. Control. 2020, 62, 101986.

[8] Pruthi, J.; Khanna, K.; Arora, S. Optic Cup segmentation from retinal fundus images using Glowworm Swarm Optimization for glaucoma detection. Biomed. Signal Process. Control 2020, 60, 102004.

[9] Kirar, B.S.; Reddy, G.R.S.; Agrawal, D.K. Glaucoma Detection Using SS-QB-VMD-Based Fine Sub-Band Images from Fundus Images. IETE J. Res. 2021, 1–12.

[10] Qureshi, I.; Khan, M.A.; Sharif, M.; Saba, T.; Ma, J. Detection of glaucoma based on cup-to-disc ratio using fundus images. Int. J. Intell. Syst. Technol. Appl. 2020, 19, 1–16.

[11] Guo, J.; Azzopardi, G.; Shi, C.; Jansonius, N.M.; Petkov, N. Automatic Determination of Vertical Cup-to-Disc Ratio in Retinal Fundus Images for Glaucoma Screening. IEEE Access 2019, 7, 8527–8541.

[12] Martins, J.; Cardoso, J.; Soares, F. Offline computer-aided diagnosis for Glaucoma detection using fundus images targeted at mobile devices. Comput. Methods Programs Biomed. 2020, 192, 105341.

[13] Nayak, D.R.; Das, D.; Majhi, B.; Bhandary, S.V.; Acharya, U.R. ECNet: An evolutionary convolutional network for automated glaucoma detection using fundus images. Biomed. Signal Process. Control 2021, 67, 102559.

[14] Shinde, R. Glaucoma detection in retinal fundus images using U-Net and supervised machine learning algorithms. Intell. Med. 2021, 5, 100038.

[15] Song, W.T.; Lai, I.-C.; Su, Y.-Z. A Statistical Robust Glaucoma Detection Framework Combining Retinex, CNN, and DOE Using Fundus Images. IEEE Access 2021, 9, 103772–103783.

[16] Hemelings, R.; Elen, B.; Barbosa-Breda, J.; Lemmens, S.; Meire, M.; Pourjavan, S.; Vandewalle, E.; Van De Veire, S.; Blaschko, M.B.; De Boever, P.; et al. Accurate prediction of glaucoma from colour fundus images with a convolutional neural network that relies on active and transfer learning. Acta Ophthalmol. 2019, 98, e94–e100.

[17] Ovreiu, S.; Paraschiv, E.-A.; Ovreiu, E. Deep Learning & Digital Fundus Images: Glaucoma Detection using DenseNet. In Proceedings of the 2021 13th International Conference on Electronics, Computers and Artificial Intelligence (ECAI), Pitesti, Romania, 1–3 July 2021.

[18] Serte, S.; Serener, A. Graph-based saliency and ensembles of convolutional neural networks for glaucoma detection. IET Image Process. 2020, 15, 797–804.

[19] Nazir, T.; Irtaza, A.; Starovoitov, V. Optic Disc and Optic Cup Segmentation for Glaucoma Detection from Blur Retinal Images Using Improved Mask-RCNN. Int. J. Opt. 2021, 2021, 6641980.

[20] Nazir, T.; Irtaza, A.; Javed, A.; Malik, H.; Hussain, D.; Naqvi, R.A. Retinal Image Analysis for Diabetes-Based Eye Disease Detection Using Deep Learning. Appl. Sci. 2020, 10, 6185.

[21] V. Badrinarayanan, A. Kendall, and R. Cipolla, “Segnet: a deep convolutional encoder-decoder architecture for image segmentation,” IEEE Transactions on Pattern Analysis and Machine Intelligence, vol. 39, no. 12, pp. 2481–2495, 2017.

[22] J. Gao, Y. Jiang, H. Zhang, and F. Wang, “Joint disc and cup segmentation based on recurrent fully convolutional network,” PLoS One, vol. 15, no. 9, article e0238983, 2020.

[23] H. Fu, J. Cheng, Y. Xu et al., “Disc-aware ensemble network for glaucoma screening from fundus image,” IEEE Transactions on Medical Imaging, vol. 37, no. 11, pp. 2493–2501, 2018.

[24] C. W. Pan, T. Y. Wong, L. Chang et al., “Ocular biometry in an urban Indian population: the Singapore Indian eye study (SINDI),” Investigative Ophthalmology & Visual Science, vol. 52, no. 9, pp. 6636–6642, 2011.

[25] S. Wang, L. Yu, X. Yang, C. W. Fu, and P. A. Heng, “Patchbased output space adversarial learning for joint optic disc and cup segmentation,” IEEE Transactions on Medical Imaging, vol. 38, no. 11, pp. 2485–2495, 2019.

[26] https://www5.cs.fau.de/research/data/fundus-images/X

[27] http://medimrg.webs.ull.es/research/retinal-imaging/rim-one/

[28] Z. Guo, L. Zhang, and D. Zhang, ―A completed modeling of local binary pattern operator for texture classification,‖ IEEE Trans. On Image Processing, vol. 19, no. 6, pp. 1657-1663, 2010.

[29] Ding, S., Xu, X., & Nie, R. (2014). Extreme learning machine and its applications. Neural Computing and Applications, 25(3), 549-556.